Pergamon

Geochimica et Cosmochimica Acta, Vol. 61, No. 18, pp. 3927–3936, 1997

0016-7037/97 $17.00 + .00

PII S0016-7037(97)00198-1

Calculated solution energies of heterovalent cations in forsterite and diopside: Implications for trace element partitioning

J. A. PURTON,[1,2] N. L. ALLAN,[1] and J. D. BLUNDY[2]

[1]School of Chemistry, University of Bristol, Cantock's Close, Bristol BS8 1TS, UK
[2]CETSEI, Department of Geology, University of Bristol, Wills Memorial Building, Bristol BS8 1RJ, UK

(*Received January* 28, 1997; *accepted in revised form May* 21, 1997)

Abstract—Solution energies are calculated for a wide range of heterovalent impurities in forsterite and diopside, using atomistic simulation techniques and a consistent set of interatomic potentials to represent the non-Coulombic interactions between the ions. The calculations allow explicitly for ionic relaxation. Association between a charged defect and its compensating defect(s) cannot be neglected at low temperatures; however, at concentrations of 10–100 ppm a large proportion will be dissociated at temperatures above 1000 K. The variation of calculated solution energy with ion size reflects the variation in the relaxation energies, and often shows a parabolic variation with ionic radius. For the pure mineral, the calculated solution energies always show a minimum at a radius corresponding to that of the host cation; for impure clinopyroxene (with <1 Ca per formula unit) the optimum cation radius varies with composition, as observed experimentally. A marked variation in the calculated solution energies for trivalent trace elements is predicted depending on which alkali-metal cation is the compensating defect. At the M1 site in diopside the lowest calculated solution energy is for trivalent ions coupled with the substitution of a Na^+ ion on the M2 site, i.e. $M^{3+}(M1)/Na^+(M2)$; at M2 it is $X^{3+}(M2)/Na^+(M2)$. $X^{3+}(M2)/Li^+(M1)$ is the lowest energy pairing for forsterite.

1. INTRODUCTION

Trace element partition between coexisting phases is crucial to many geochemical and industrial processes and an understanding of the physical and chemical controls on the distribution of trace metals has implications for processes as wide ranging as Earth differentiation and radioactive waste management. The solubility of a dopant cation in a mineral depends on the charge and size of the element (Goldschmidt, 1937) in addition to the pressure (P), temperature (T), and phase composition (x). Recent advances in analytical techniques have lead to extensive experimental investigations of trace element partitioning between minerals and melts in simple silicates (e.g., Hart and Dunn, 1993; Kennedy et al., 1993; Beattie, 1994; Blundy and Wood, 1994; Hauri et al., 1994; LaTourette et al., 1995). The present study integrates these experimental approaches with modern computer atomistic simulation techniques for the energetics of heterovalent element substitution into crystal lattices.

In a previous paper, Paper I (Purton et al., 1996), we have presented a theoretical study, using modern computer simulation techniques, of the solution energies of isovalent substitution of cations in a range of minerals (calcium oxide, diopside, enstatite, and forsterite). We now turn our attention to heterovalent substitution of trivalent and monovalent cations in two minerals—the olivine forsterite (Mg_2SiO_4) and the clinopyroxene diopside ($CaMgSi_2O_6$). Compared to isovalent substitution the incorporation of ions with a charge different from that of the host cation (e.g., the substitution of Ca^{2+} by La^{3+}) presents several additional problems. First, the polarization of the lattice resulting from a charged defect must be considered . In addition, to maintain charge neutrality, the charged defect must be accompanied by a charge-compensating defect(s). In the minerals studied here, this will in general be either a vacancy (e.g., two tripositive ions and a divalent-cation vacancy replacing three divalent cations) or another heterovalent cation (e.g., two Ca^{2+} ions may be replaced by La^{3+} and Li^+, or Ca^{2+} and Si^{4+} may be replaced together by La^{3+} and Al^{3+}, respectively). As a result, any theoretical study must take into account both substituent and possible compensating defects and their spatial arrangement.

The aim of this paper is to consider the fundamental physics and chemistry underlying the incorporation of cation impurities. With this in mind, we have not attempted at this stage to calculate mineral-melt partition coefficients directly, but rather calculate solution energies in the dilute limit for a wide range of possible aliovalent substitutions. Here, we concentrate on the solution energies of trace element cations in the solid mineral and consider the energetics of the appropriate exchange reactions. For example, for CaO in forsterite (Paper I), the exchange reaction is

$$CaO(s) + MgMgSiO_4(s) = MgO(s) + CaMgSiO_4(s) \quad (1)$$

and for Y^{3+} in forsterite possible charge compensation mechanisms can be expressed in a similar manner,

$$Li_2O(s) + Y_2O_3(s) + 2MgMgSiO_4(s) = 2MgO(s) + 2YLiSiO_4(s) \quad (2a)$$

$$2Y_2O_3(s) + 3MgMgSiO_4(s) = 6MgO(s) + 3Y_{4/3}\square_{2/3}SiO_4(s) \quad (2b)$$

$$Al_2O_3(s) + Y_2O_3(s) + 2MgMgSiO_4(s) = 2MgO(s) + 2SiO_2(s) + 2YMgAlO_4(s) \quad (2c)$$

where $\square$ denotes a cation vacancy. It is straightforward to

write similar equations for other possible charge-balance mechanisms.

The equilibrium constant, K, for any such reaction is related to the free energy change for the reaction, $\Delta G_{exchange}$, via

$$-RT \ln K = \Delta G_{exchange} = \Delta H_{exchange} - T\Delta S_{exchange} \quad (3)$$

where $\Delta H_{exchange}$, and $\Delta S_{exchange}$ are the corresponding enthalpy and entropy change, respectively. $\Delta S_{exchange}$ reflects the difference in configurational entropy together with the change in vibrational entropy of the solid. In this paper, we consider the solution energies in the dilute limit and concentrate on $\Delta H_{exchange}$. The energetics for different compensation mechanisms (e.g., reactions 2a,b,c) in this limit are also considered in detail.

2. THEORETICAL METHODS

The theoretical methods (Catlow and Mackrodt, 1982) used in the present paper have been used recently to study a wide range of doped ternary systems with perovskite-related structures (e.g., the cuprates La_2CuO_4 and Nd_2CuO_4; Allan and Mackrodt, 1993) and on a variety of silicate minerals (e.g., Catlow and Price, 1990; Patel et al., 1991; Pavlides and Catlow, 1994). Consequently, we present only a short summary. The calculations are formulated within the framework of an ionic model—integral ionic charges are assigned based on accepted chemical valence and electron counting, i.e., 2+ for Ca and Mg, 4+ for Si, and 2− for O. The shell model of Dick and Overhauser (1958) is used to take some account of electronic polarisation. The defect energies are obtained by the customary two region approach (Catlow and Mackrodt, 1982) in which the total energy of the defective system is minimized by variation of the nuclear positions and shell displacements around the defect. In the inner region immediately around the defect, consisting of ~400 species, the forces are determined explicitly to obtain the relaxations. In the outer region, these are estimated using the Mott-Littleton approximation (Mott and Littleton, 1938; Lidiard, 1989).

The success of any simulation relies on the accuracy and transferability of the short-range interatomic potentials. We have used a well-established potential set based on the transferability of potentials from SiO_2 (Sanders et al., 1984) and the constituent binary oxides (Lewis and Catlow, 1985). This model has been demonstrated to reproduce accurately the structure and thermodynamic properties of a wide range of mineral structures (Patel et al., 1991; Winkler et al., 1991). The calculated cell parameters for the minerals studied in this paper are given in Table 2 of Paper 1 and so are not reproduced here. Buckingham potentials for the interaction between the dopant cations and O were obtained either from Lewis and Catlow (1985) or from fitting to the structure (and, if available, the elastic properties) of the binary oxide. The full set of potentials are given in Table 1.

As in our previous paper, the defect energies reported here are internal energies in the athermal limit (i.e., 0 K in the absence of lattice vibrations). However, defect enthalpies usually show only a small temperature dependence, and to a good approximation defect enthalpies (h_P) at elevated temperatures often equal the change in internal energy (u_V) at 0 K ($h_P(T) \approx u_V(0)$), thus explaining why calculated energies so often agree well with enthalpies measured at high temperatures. The theoretical justification for this and some examples have been discussed by Catlow et al. (1981) and Allan et al. (1987).

In geochemical studies, partitioning is often related to the ionic radius of the substituent cation. For presentation purposes and the discussion of trends, we use the appropriate ionic radius for the coordination number of the atom of interest, from Shannon (1976). For the ionic radii, we have taken the values for sixfold coordination, except for substitution at the M2 site in diopside where the values for eightfold coordination are more appropriate. It is important to note that the simulation approach makes no use of the concept of ionic radius and so avoids all the problems associated with the precise definition of, and suitable values for, this quantity. This is even more acute for coupled substitutions with heterovalent trace elements where there are two or more defects possibly strongly associated since the effective radius in such situations is not at all clear.

Table 1. Interatomic potential parameters, in addition to those of Paper 1. Cation/cation potentials are purely Coulombic. A short-range cutoff of 12 Å was used throughout.

Interaction	A (kJ mol^{-1})	ρ (Å)	C (kJ mol^{-1} Å^6)
Li^+/O^{2-}	25331.2	0.3476	0.0
Na^+/O^{2-}	122231.1	0.3065	0.0
K^+/O^{2-}	65652.1	0.3798	0.0
Rb^+/O^{2-}	88706.4	0.3772	0.0
Cs^+/O^{2-}	62676.656	0.4142	6207.8
Sc^{3-}/O^{2-}	125372.6	0.3312	0.0
La^{3-}/O^{2-}	138909.5	0.3651	0.0
Nd^{3-}/O^{2-}	133139.7	0.3601	0.0
Eu^{3+}/O^{2-}	131026.6	0.3556	0.0
Gd^{3+}/O^{2-}	128981.1	0.3551	0.0
Ho^{3+}/O^{2-}	130274.0	0.3487	0.0
Lu^{3+}/O^{2-}	129974.9	0.3430	0.0
Yb^{3+}/O^{2-}	126356.8	0.3462	0.0

3. RESULTS

3.1. Relaxation and Defect Energies for Isolated Defects

The calculated defect energies for isolated monovalent and trivalent impurities in forsterite and diopside, allowing for *full relaxation* of the lattice around each defect, are plotted in Fig. 1. The results for the isovalent dopants considered in Paper 1 are also shown. For a given cation radius, the defect energies follow the order monovalent > divalent > trivalent. The defect energies for all the monovalent ions are positive and for the trivalent ions, negative, exactly as expected from classical electrostatics. Of course, this does not mean that the overall solution energies for univalent ions are all positive and are all negative for trivalent ions since other terms also contribute to the solution energies. The variation of defect energy with ionic radius is approximately linear in all cases (Fig. 1); for both compounds, the slope of these lines increases in the order

monovalent < divalent < trivalent.

The defect energies in forsterite (M1 and M2) generally show a slight preference of univalent cations for the M1 site and the others, for the M2 site. In diopside, the defect energies are lower for univalent cations at the M1 site (Mg) than at M2 (Ca), whereas the opposite is true for trivalent and divalent impurities. For the reasons discussed below, this does not necessarily mean that univalent cations will substitute at M1 and the others at M2.

One of the important contributions to the overall defect energy is the *relaxation energy*, which is the energy released as the ions move to accommodate the new cation. The values of the relaxation energy for the isolated defects are shown in Fig. 2 for substitution at M1 and M2 sites in diopside.

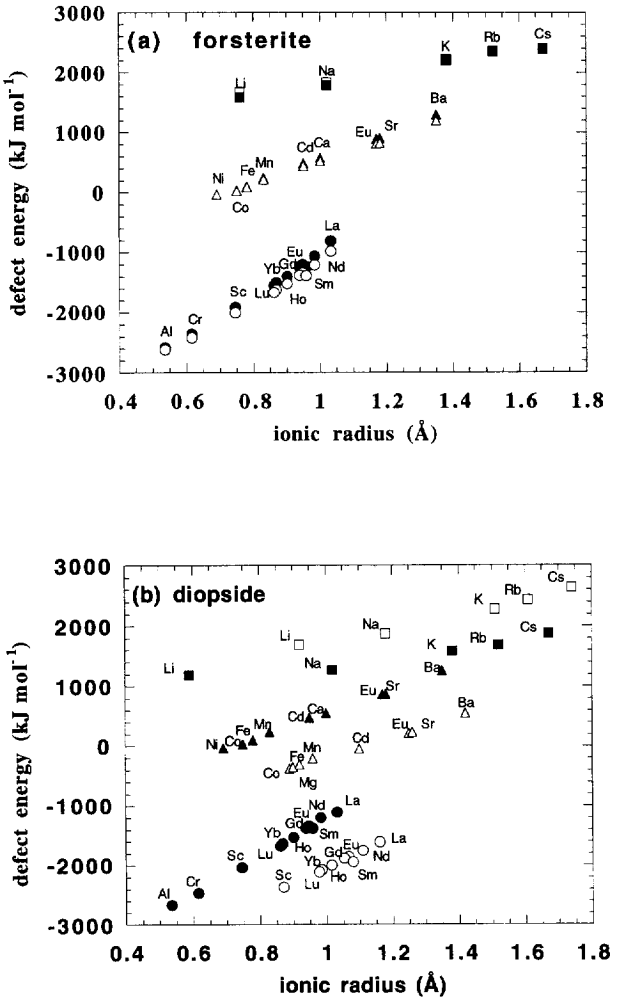

Fig. 1. Calculated defect energies (kJ mol^{-1}) vs. ionic radius (Å) for isovalent and heterovalent substituents in forsterite and diopside. Open symbols denote substitution at the M2 site; filled symbols, substitution at M1 (this notation is adhered to for all the figures). Only the lowest defect energy is plotted.

For forsterite, the relaxation energies are similar to those for the M1 site in diopside (Fig. 2a). It is important to note that, unlike for the isovalent substituents in Paper 1, the relaxation energy for charged defects is always greater than zero, due to the polarisation of the lattice. For isovalent dopants, the minimum relaxation energy occurs, in all cases we have studied, at the radius closest to that of the host cation (i.e., Mg in the M1 site and Ca in the M2 site of diopside). The curves for the univalent and trivalent cations on the M2 site in diopside in Fig. 2b do not quite reach minima, and if present, these minima would not correspond to the ionic radius of Ca^{2+}. The relaxation energies for isovalent dopants show an approximate parabolic dependence on the ionic radius of the dopant (Paper 1). The parabolae for univalent impurities are less tight than for divalent impurities, while the 3+ curves are much tighter. For trivalent impurities in the M1 site of diopside (Fig. 2a) and the M1 and M2 sites of forsterite, the variation with relaxation energy with size is more asymmetric.

For a given dopant charge, the curvature of the parabolae varies from site to site in a fashion consistent with what is known about their relative compressibilities. For example, in diopside, the relaxation energy for cations of a given charge at the M1 site shows a tighter parabola than that for the M2 site, in keeping with experimental studies which show that the M2 site is more compressible than the M1 site (Levien and Prewitt, 1981). The analogous plots for any of the Mg sites in forsterite are similar to that for the M1 site in diopside, suggesting that it is the rigidity of the local environment rather than that of the bulk crystal that largely determines the relaxation energy (cf. the cation-anion polyhedra approach of Hazen and Finger, 1979).

3.2. Relaxation and Defect Energies for Charge Compensated Defects

As we have already stressed, electroneutrality requires that incorporation of charged defects must be accompanied by charge-compensating defect(s). For M^{3+} trace elements

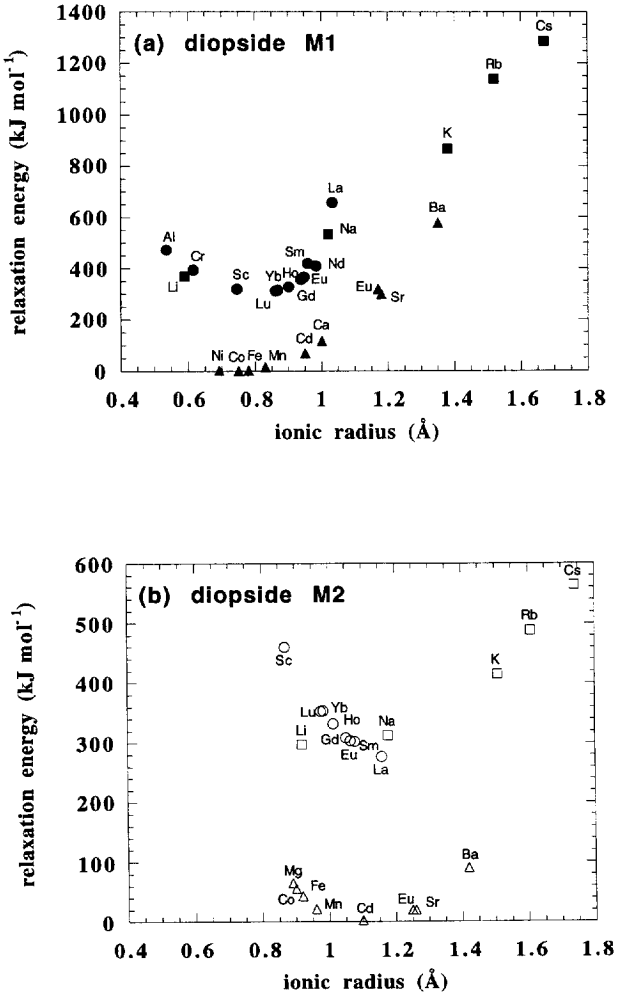

Fig. 2. Calculated relaxation energies (kJ mol^{-1}) vs. ionic radius (Å) for (isolated) isovalent and heterovalent substituents in diopside at the M1 and M2 sites.

(which at a 2+ site carry an effective positive charge), the most likely possibilities include cation vacancies or coupled substitutions such as M^+ substitution for a further divalent cation or aluminium substitution for silicon on the tetrahedral site. For M^- trace elements (which have an effective negative charge at a 2+ site), we have considered both O vacancy compensation and M^{3+} substitution for a further divalent cation.

Charge compensation may occur with two isolated defects located so remote from each other that the total energy is the sum of the isolated defects, i.e.,

$$E(M^{3-}) + E(M^-) \tag{4a}$$

Alternatively two defects may be situated as close as possible to one another, allowing for the association energy between the oppositely charged defects. We denote this by

$$E(M^{3-} + M^+) \tag{4b}$$

Plots of isolated and associated defects are shown in Figs. 3 and 4, respectively. A comparison of these figures shows clearly that in the case of forsterite and the M1 site of diopside, the effect of association is large, reducing the formation energies by roughly 100 kJ mol^{-1}. This is expected from a simple calculation of the interaction between two point charges separated by 3 Å (the M1-M1 distance in these minerals) in a continuum with a dielectric constant set equal to that of a typical silicate mineral (≈6). In the M2 site, the difference in defect energies is much less and varies between ≈20 and 100 kJ mol^{-1}. This is due to the M2-M2 site separation being greater, 4.5 Å, than the M1-M1 distance, 3.2 Å.

Figure 5 shows the calculated relaxation energies for these associated defects in forsterite and diopside plotted against the trivalent cation radius. A comparison of Figs. 5 and 2 shows that the variation of relaxation energy with size is similar at the M1 site in the two situations, but quite different at the M2 site in diopside. On both sites, the relaxation energies exhibit a parabolic dependence on the ionic radius, and the minimum occurs at the radius corresponding to that of the host cation. Again, the relaxation energy for these defects is always positive and never zero, and the curvature of these parabolae is tighter on M1 than M2. It is important to note that for the associated defects at the M1 and the M2 site in forsterite and diopside, the relaxation energies are not additive and cannot be predicted simply from the separate relaxations for the isolated defects.

3.3. Solution Energies

Several factors in addition to the defect energies contribute to the solution energies for forsterite and diopside. Even though the size of the dopant ion provides a useful rule of thumb, the magnitude of the solution energy and, where there is more than one possible cation site, the mode of solution cannot always be obtained solely from a simple consideration of the size of the impurity ion. For the substitutions considered in Paper 1, it was straightforward within the spirit of the approach of Henderson and Kracek (1927) to calculate solution energies, E_{Ca} and E_{Mg}, for the reactions (cf. reaction 1),

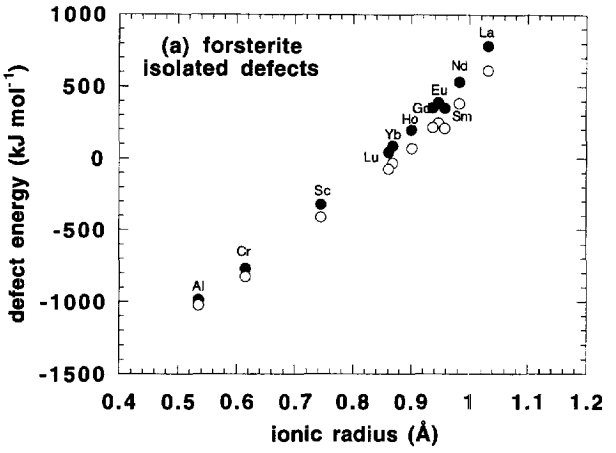

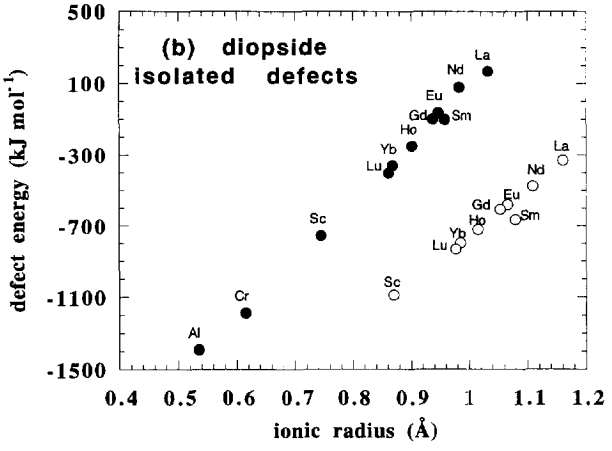

Fig. 3. Calculated defect energies (kJ mol^{-1}) vs. ionic radius (Å) for substitution by +3 substituents in forsterite and diopside. The energies plotted correspond to the sum of the *isolated* defects (+3 ion + charge-compensating defect), as described in the text (Eqn. 4a). See Fig. 6 caption for defect pairings.

$$MO + Ca_{Ca} \rightarrow M_{Ca} + CaO \tag{5a}$$

$$MO + Mg_{Mg} \rightarrow M_{Mg} + MgO \tag{5b}$$

which are written using Kröger-Vink notation (Kröger and Vink, 1956). M denotes a trace divalent cation, and subscripts Mg and Ca identify the host cation on the site of interest. Clearly these reactions involve not only the defect energies calculated above, but also the difference in lattice energies E_{latt} between the two binary oxides also involved, i.e., for Eqn. 5a:

$$E_{sol} = E(M_{Ca}) + E_{latt}(CaO) - E_{latt}(MO) \tag{5c}$$

It is somewhat more involved to extend this approach to heterovalent trace impurities since there are several possibilities depending on the mode of defect compensation. Rewriting reactions of Eqn. 2a–c, using Kröger-Vink notation, for trivalent dopants at an Mg site:

$$\tfrac{1}{2}M_2O_3 + \tfrac{1}{2}X_2O + 2Mg_{Mg} \rightarrow M^{\bullet}_{Mg} + X'_{Mg} + 2MgO$$

$$E_{sol} = E(M^{\bullet}_{Mg} + X'_{Mg}) + 2E_{latt}(MgO) - \tfrac{1}{2}E_{latt}(M_2O_3) - \tfrac{1}{2}E_{latt}(X_2O) \quad (6a)$$

$$\tfrac{1}{2}M_2O_3 + \tfrac{3}{2}Mg_{Mg} \rightarrow M^{\bullet}_{Mg} + \tfrac{1}{2}V''_{Mg} + \tfrac{3}{2}MgO$$

$$E_{sol} = \tfrac{1}{2}E(2M^{\bullet}_{Mg} + V''_{Mg}) + \tfrac{3}{2}E_{latt}(MgO) - \tfrac{1}{2}E_{latt}(M_2O_3) \quad (6b)$$

$$\tfrac{1}{2}M_2O_3 + \tfrac{1}{2}Al_2O_3 + Mg_{Mg} + Si_{Si} \rightarrow M^{\bullet}_{Mg} + Al'_{Si} + MgO + SiO_2$$

$$E_{sol} = E(M^{\bullet}_{Mg} + Al'_{Si}) + E_{latt}(MgO) + E_{latt}(SiO_2) - \tfrac{1}{2}E_{latt}(M_2O_3) - \tfrac{1}{2}E_{latt}(Al_2O_3) \quad (6c)$$

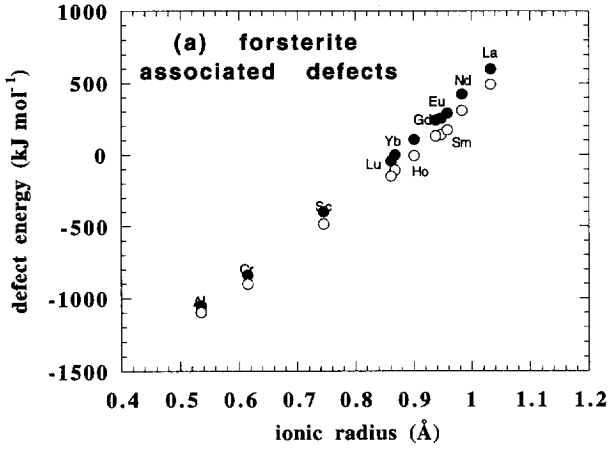

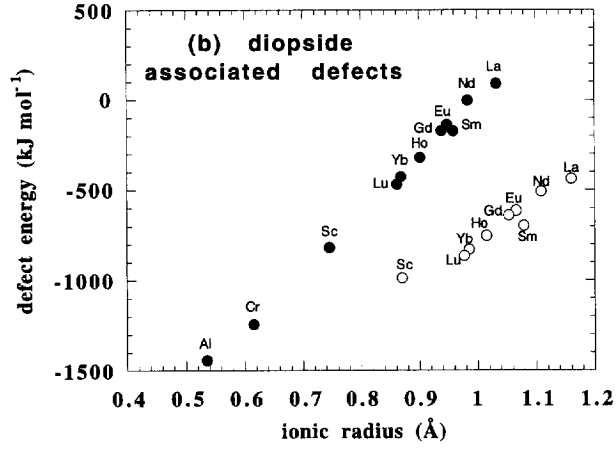

Fig. 4. Calculated defect energies (kJ mol^{-1}) vs. ionic radius (Å) for substitution by +3 substituents in forsterite and diopside. The energies plotted correspond to the sum of the *associated* defects (+3 ion + charge-compensating defect), as described in the text (Eqn. 4b). Defect pairings as in Fig. 3.

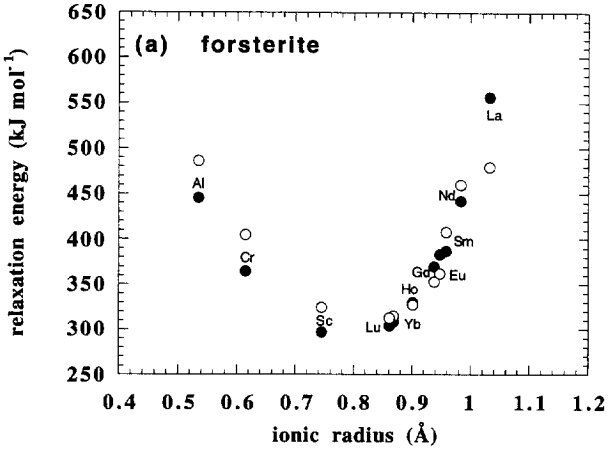

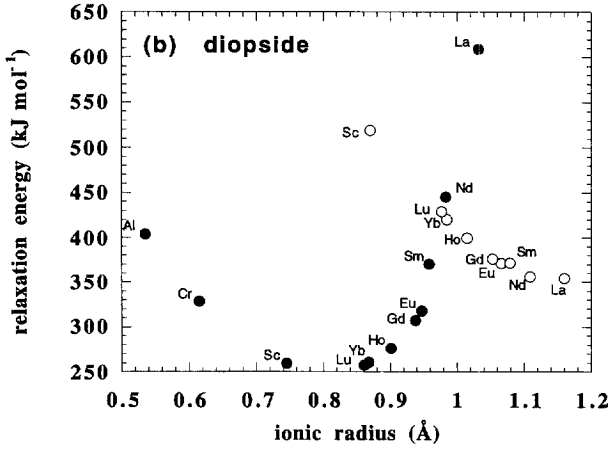

Fig. 5. Calculated relaxation energies (kJ mol^{-1}) vs. ionic radius (Å) for substitution by +3 substituents in forsterite and diopside. The energies plotted correspond to the sum of the associated defects (+3 ion + charge-compensating defect), as described in the text (Eqn. 4b). As in Fig. 1, open symbols denote M2; filled symbols, M1.

For a monovalent dopant, in addition to reaction 6a, a further possibility is

$$\tfrac{1}{2}X_2O + \tfrac{1}{2}O_O + Mg_{Mg} \rightarrow X'_{Mg} + \tfrac{1}{2}V^{\bullet\bullet}_{O} - MgO$$

$$E_{sol} = \tfrac{1}{2}E(2X'_{Mg} + V^{\bullet\bullet}_{O}) + E_{latt}(MgO) - \tfrac{1}{2}E_{latt}(X_2O) \quad (6d)$$

The corresponding equations for incorporation at the Ca site follow immediately.

As part of this work, we have also investigated compensation of defects with an effective positive (negative) charge by O interstitials (vacancies) and for trivalent impurities the energetics of trivalent substitution for Mg coupled with Al substitution for Si. These are all much higher in energy than the reactions listed above and our results for 3+ ions in forsterite do not support the suggestion of Colson et al. (1989) that Sc^{3+} and Yb^{3+} ions are compensated by cation vacancies, which have large formation energies. Neither do our results support the suggestion of Beattie (1994) that the

favoured compensation mechanism for olivine is coupled substitution $M^{3+}/Al^{3+}(Si)$, according to Eqn. 6c. This is clear from a comparison of Figs. 6 and 7, which shows that for forsterite, the solution energies for Al^{3+} compensation are typically 200 kJ mol^{-1} larger than that for Li^+ compensation.

Figure 6 shows the variation of solution energy (per mole of dopant M or X ions) with ionic radius for forsterite and diopside. For each dopant only, that mode of solution which gives the lowest solution energy is plotted, which in every case involves the associated defect pair between the impurity and its compensating defect. For forsterite (Fig. 6a), the lowest mode of solution is for the trivalent ion to occupy the M2 site with a compensating Li^+ cation on the M1 site. The solution energy reflects both the distance between the ions and the elasticity of the site. The $X^{3+}(M2)/Li^+(M1)$ configuration is lower in energy than the $X^{3+}(M2)/Li^+(M2)$ since the smallest M1-M2 distance is 3.26 Å compared with 3.89 Å for the M2-M2 separation (note the distances are for the perfect relaxed structure). The solution energy for $X^{3+}(M1)/Li^+(M1)$ is greater still in energy due to the rigidity of the M1 site, which is therefore less tolerant of trivalent dopant cations, despite the smallest M1-M1 distance being only 2.99 Å. In diopside (Fig. 6b), the most favoured solution mechanisms are different since the M1 and M2 sites are occupied by different cations. At the M1 site, the lowest solution energy is observed for trivalent ions coupled with the substitution of a Na^+ ion on the M2 site, i.e., $M^{3+}(M1)/Na^+(M2)$. In contrast to forsterite, the lowest energy for substitution of a trivalent ion on the M2 site is coupled with the substitution of a Na^- ion for a second Ca^{2+} ion, i.e., $X^{3+}(M2)/Na^+(M2)$.

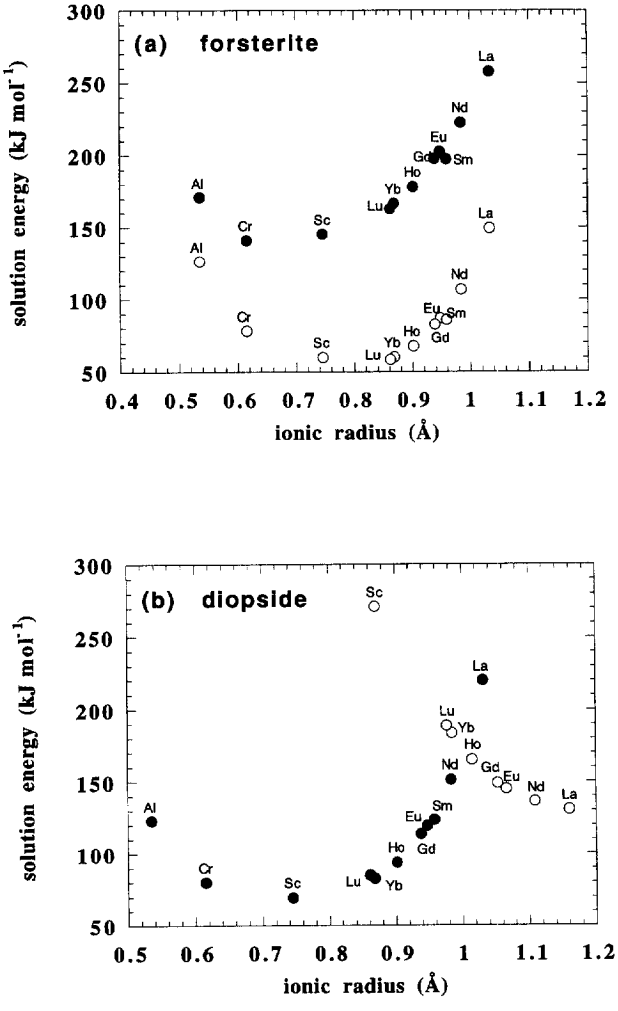

Fig. 6. Calculated solution energies (kJ mol^{-1}) vs. ionic radius (Å) for substitution by +3 ions in forsterite and in diopside. For each dopant, only that mode of solution which gives the lowest solution energy (Eqn. 6a) is plotted, as described as in the text. For forsterite this is $X^{3+}(M2)/Li^+(M1)$ and for diopside, $M^{3+}(M1)/Na^+(M2)$ and $X^{3+}(M2)/Na^+(M2)$.

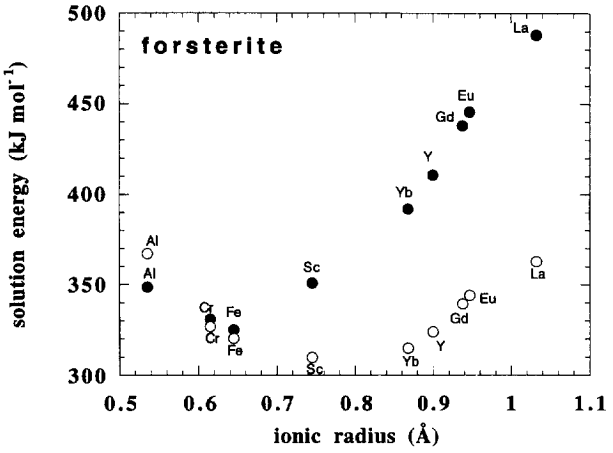

Fig. 7. Calculated solution energies (kJ mol^{-1}) vs. ionic radius for trivalent ions in forsterite, assuming Al^{3+} compensation on the tetrahedral site (as in Eqn. 6c). Compare Fig. 6a.

For 3+ ions at the M1 and M2 sites in diopside and forsterite, the calculated variation of solution energy with ionic radius is parabolic with, as expected, a minimum at the "optimum" radius, which is approximately that of the host cation (Mg or Ca). All our calculated solution energies agree with the rule of thumb that the most soluble dopants are those closest in size to the host cation. For a given charge, the origin of the parabolic dependence is not the variation of the energies of the defect pair with ionic radius (which increases approximately linearly with ionic radius – Fig. 4) nor the variation of the difference in lattice energy between M_2O_3/MgO (M_2O_3/CaO) (which decreases with ionic radius), but is the sum of these two effects. The variation of the solution energies from site to site mimics that of the relaxation energies as described above, testifying once more to the importance of the local environment in controlling substitution.

An interesting conclusion to emerge from our study is that we predict a marked variation in the calculated solution energies for trivalent trace elements depending on which alkali-metal cation is the compensating defect, as shown graphically in Fig. 8. The solution energies are displayed for univalent cations X^+ in forsterite ($X^+(M1)/Sc^{3+}(M2)$) and diopside ($Lu^{3+}(M1)/X^+(M2)$), which are the lowest

energy modes of solution. The most favourable univalent cations for forsterite and diopside are Li^+ and Na^+, respectively, which would be expected from cation size arguments. We emphasise that the nature of the charge balancing cations is also important in the melt, and this would need to be taken into account in a full treatment.

4. CRYSTAL CHEMICAL EFFECTS AND CONFIGURATIONAL ENTROPY

In this section we assess briefly to what extent these findings are influenced by the inclusion of crystal compositional effects and configurational entropy.

So far we have not taken into account crystal compositional effects. For example, our simulations are performed on perfectly stoichiometric, ordered $CaMgSi_2O_6$. In nature, most natural clinopyroxene (cpx) compositions for which partitioning data are available contain appreciable $MgSiO_3$ in solid solution. Consequently, both Mg and Ca occur on the M2 site. In order to examine the effect of this on the calculated solution energies, we have performed defect calculations on a diopside $2 \times 2 \times 1$ supercell with 1/16 of the Ca^{2+} ions on M2 replaced by Mg^{2+} ions (i.e., $Ca_{15/16}Mg_{17/16}Si_2O_6$). There are several possibilities for the incorporation of heterovalent trace elements according to

$$\tfrac{1}{2}M_2O_3 + \tfrac{1}{2}X_2O + Mg_{M1} + Mg_{M2} \rightarrow M^{\cdot}_{M1} + X'_{M2} + 2MgO \quad (7a)$$

$$\tfrac{1}{2}M_2O_3 + \tfrac{1}{2}X_2O + Mg_{M2} + Ca_{M2} \rightarrow M^{\cdot}_{M2} + XM2 + MgO + CaO \quad (7b)$$

$$\tfrac{1}{2}M_2O_3 + \tfrac{1}{2}X_2O + 2Mg_{M2} \rightarrow M^{\cdot}_{M2} + X'_{M2} + 2MgO \quad (7c)$$

Figure 9 shows the resulting solution energies for the reaction 7a and c, assuming associated defects. Reaction 7b is always higher in energy than 7c and so these energies are not shown. The solution energies for reaction 7a and c (Fig. 9) are lower than the solution energies reported in the last section (compare Fig. 6b). The solution energies assuming isolated defects are reduced by similar amounts. The lowest solution energies correspond to reaction 7c.

The results clearly demonstrate the possible importance of crystal chemical effects since rare-earth elements, except Lu and Yb, are now predicted to sit on the M2 site in preference to M1, and the minimum in the solution energy is shifted to a smaller "optimum" ionic radius, i.e., 1.1 Å (Fig. 9) vs. >1.16 Å (Fig. 6b). The occurrence of lanthanides on M2 in cpx is consistent with the observed preference of these elements for cpx vs. coexisting opx, which lacks a large M2 site (e.g., Pun and Papike, 1995).

Neither have we made any mention of configurational entropy. Effects due to this will not be large enough to influence the site preference of the lanthanides but can have a profound influence upon the extent to which compensating defects are associated at high equilibration temperature observed in natural rocks. Turning to the defect concentrations

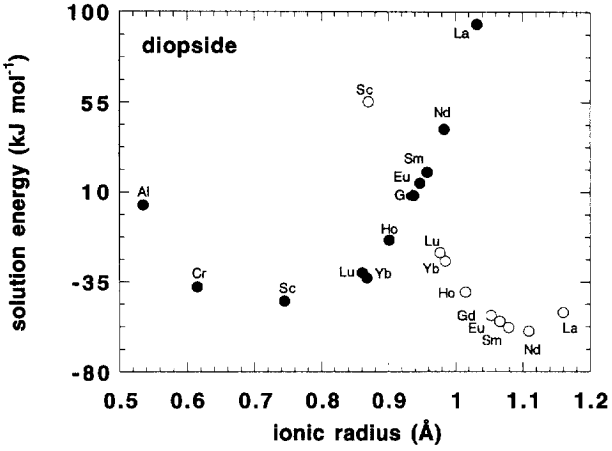

Fig. 9. Calculated solution energies (kJ mol^{-1}) vs. ionic radius (Å) for +3 ions in an idealised diopside containing an excess of Mg^{2+} ions over Ca^{2+} ions ($Ca_{15/16}Mg_{17/16}Si_2O_6$). The solution energies correspond to Eqn. 7a and c in the text.

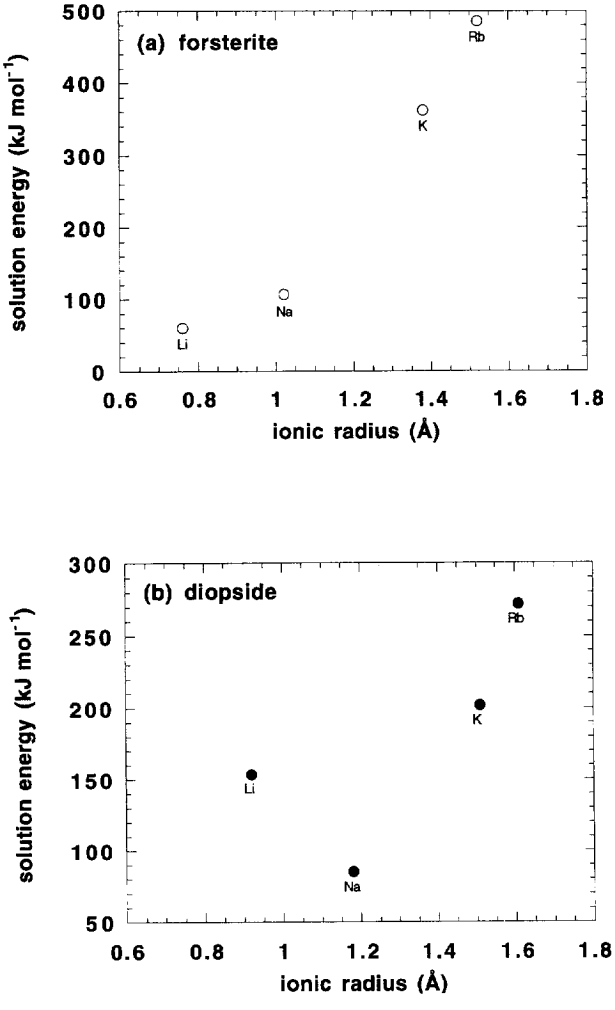

Fig. 8. Calculated solution energies (kJ mol^{-1}) vs. ionic radius (Å) for substitution by +1 ions in forsterite and in diopside, as discussed in the text (Eqn. 6a).

themselves, we can apply the standard statistical thermodynamic treatment (e.g., Fuller, 1972). Given, as calculated earlier, typical association energies in the range 30–100 kJ mol^{-1}, at experimental temperatures ($\approx$1400 K) and above the fraction of associated defect pairs for a typical impurity concentration of 10–100 ppm, will be very small. This has implications for the derivation of activity-composition relations in high temperature trace-element bearing minerals. These ideas will be developed further in a later paper.

5. IMPLICATIONS FOR TRACE ELEMENT PARTITIONING

Direct comparison with experimental partition coefficients is not possible since we have neglected finite concentration effects and the melt. Nevertheless, the reactions we have studied (e.g., reaction 1) are similar to those used in the approach of Henderson and Kracek (1927) to trace-element partitioning. It is worthwhile to compare the trends observed experimentally (Fig. 10) with those in our calculated solution energies.

Some trends are common to both calculated solution energies and experimental partition coefficients, D, defined as the concentration ratio of trace element in mineral to that in melt. For ions of comparable size, +1 and +3 cations are both calculated to be less soluble than the isovalent impurities considered in our earlier work. This is generally, but not always, observed in the experimental partitioning results. For example, La and Na are always observed to have lower Ds than Ca in cpx (Blundy and Wood, 1994; Hauri et al., 1994). Both the calculated solution energies (Figs. 6 and 9) and the values of D for isovalent series of cations show a parabolic dependence on ionic radius (Onuma et al., 1968; Blundy and Wood, 1994). For both, too, the curvature of the parabolae tends to increase with increasing charge.

A clear difference between the variation in the calculated solution energies and that in the values of D is that the lowest solution energy always occurs at a radius corresponding to that of the host cation. For example, the experimental maximum D in diopside for +3 ions at the M2 site appears to occur for an ionic radius $\approx$1.0 Å (Wood and Blundy, 1997), whereas the calculated minimum in the solution energies (excluding crystal chemical effects) is at a much larger radius—similar to that of Ca^{2+} in eightfold coordination. In stoichiometric, ordered diopside, all the 3+ cations smaller than and including Sm^{3+} are predicted to substitute at the M1 site, whereas experimentally the REEs appear to substitute for Ca^{2+} (M2). If we include crystal chemical effects, explicitly placing Mg^{2+} ions on some Ca^{2+} sites, the minimum in the solution energies is shifted to a smaller ionic radius and the REEs are more soluble at the M2 site. For our calculated solution energies, the optimum lanthanide changes from La^{3+} to Nd^{3+}. However, the rare-earth element with the largest value of D is Dy. Experiment as well as calculation shows the optimum cation radius can be a sensitive function of crystal chemistry, e.g., Wood and Blundy (1997) show that the optimum cation radius for the M2 in diopside decreases with increasing Al^{3+} content and decreasing Ca content of the cpx.

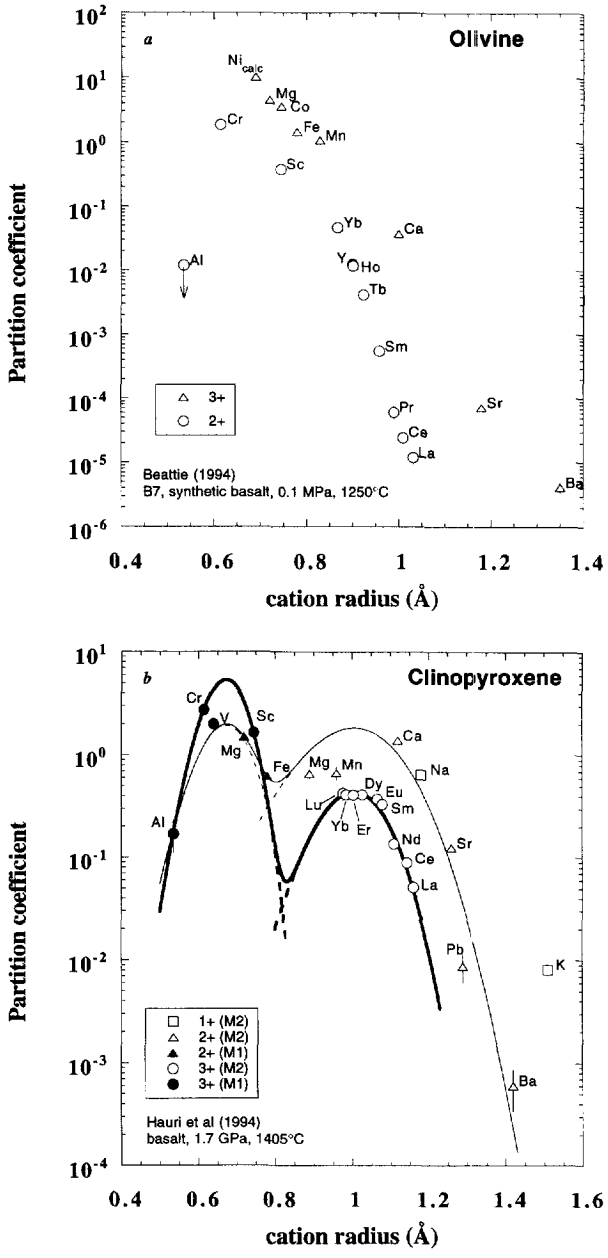

Fig. 10. Experimentally determined mineral-melt partition coefficients for a range of cations plotted vs. ionic radius for the minerals (a) olivine (Beattie, 1994) and (b) clinopyroxene (Hauri et al., 1994). One standard-deviation analytical error bars are smaller than the symbol except where shown. The values for Al on M1 and Mg on M2 in clinopyroxene and Al on M1 in olivine are calculated from the structural formula. The value of D_{Ni} for olivine is calculated for the experimental conditions and composition from the expression in Beattie et al. (1991). In (b), curves are fitted to the data as described in Blundy and Wood (1994) to illustrate the presence of two maxima corresponding to the M1 and M2 sites. The two broken curves are fitted to the individual sites D_{M1} and D_{M2}, while the solid curve denotes the summed variation $D_{M1}+D_{M2}$. The bold lines are for 3+ cations and the thin lines for 2+ cations.

Differences between the trends displayed by the calculated solution energies and the experimental partition coefficients indicate the need for a more elaborate model, taking into

account factors such as melt structure, entropy, and cation ordering. In addition, at this stage, our calculations cannot take account of variations in crystal field or Jahn-Teller energies with site geometry. These can be important, for example, in Fig. 10b where the partition coefficient for Cr^{3+} is larger than that for Sc^{3+}.

6. CONCLUSIONS

In this paper we have calculated solution energies for a wide range of heterovalent impurities in forsterite and diopside, using atomistic simulation techniques and a consistent set of interatomic potentials to represent the non-Coulombic interactions between the ions. It is worth stressing that our approach relies only on the transferability of potentials between different structures and makes no assumptions concerning either the elasticity or the anisotropic nature of the mineral. The local environment is taken into account as a matter of course, and there is no need to adopt any empirical fitting procedure. The calculations allow for the effects of the polarization of the lattice by the charged defects and explicitly for ionic relaxation close to the dopant.

Our results show that in these minerals association between a charged defect and its compensating defect(s) cannot be neglected at low temperatures. Preliminary calculations suggest that at concentrations of 10–100 ppm, a large proportion will be dissociated at temperatures above 1000 K. The variation of calculated solution energy with ion size reflects the variation in the relaxation energies and often shows a parabolic variation with ionic radius. For the pure mineral, the calculated solution energies always show a minimum at a radius corresponding to that of the host cation, even though there are several terms contributing to the overall solution energy—for impure cpx, we note that the optimum cation radius varies with composition, as observed experimentally. We predict a marked variation in the calculated solution energies for trivalent trace elements, depending on which alkali-metal cation is the compensating defect. For example, for a given 3+ ion, the solubility should show a marked difference according to whether Na^+ or K^+ is also present. There is clearly an urgent need for more experimental data with which to compare our results, e.g., direct measurements as to the site preferences of trace elements in diopside.

At the M1 site in diopside, the lowest calculated solution energy is for trivalent ions coupled with the substitution of a Na^+ ion on the M2 site, i.e., $M^{3+}(M1)/Na^-(M2)$; at M2, it is $X^{3+}(M2)/Na^+(M2)$. $X^{3+}(M2)/Li^+(M1)$ is the lowest energy pairing for forsterite.

For forsterite, the trends in the calculated values of the solution energies in the main reflect those in the available olivine-melt trace element partition coefficients. This is not so when comparing pure diopside with experimental cpx-melt Ds, where it appears that factors such as the variations in crystal composition, melt composition, and temperature effects must be explicitly considered. Future work will concentrate on direct simulations of both melt and mineral so as to calculate trace element partition coefficients directly, considering also a range of defect concentrations, temperature effects, and configurational entropy.

Acknowledgments—This work was funded by NERC grant GR3/09772. JDB is also grateful for financial support through a research fellowship provided by the Royal Society (516002). Calculations were performed on dedicated workstations funded by EPSRC (grant GR/K48686) and the Royal Society. We thank A. Navrotsky for a helpful review.

REFERENCES

Allan N. L. and Mackrodt W. C. (1993) Simulation studies of structural and defect properties of high temperature superconducting materials. *Adv. Solid State Chem.* **3**, 221–269.

Allan N. L., Mackrodt W. C., and Leslie M. (1987) Calculated point-defect entropies in MgO. *Advances in Ceramics* **23**, 257–271.

Beattie P. (1994) Systematics and energetics of trace-element partitioning between olivine and silicate melts: Implications for the nature of mineral/melt partitioning. *Chem. Geol.* **117**, 57–71.

Beattie P. D., Ford C. E., and Russell D. G. (1991). Partition coefficients for olivine-melt and orthopyroxene-melt systems. *Contrib. Mineral. Petrol.* **109**, 212–224.

Blundy J. D. and Wood B. J. (1994) Prediction of crystal-melt partition coefficient from elastic moduli. *Nature* **372**, 452–454.

Catlow C. R. A. and Mackrodt W. C. (1982) Theory of simulation methods for lattice and defect energy calculations in crystals. In *Computer Simulation of Solids* (ed. C.R.A. Catlow and W.C. Mackrodt), pp. 3–20. Springer-Verlag.

Catlow C. R. A. and Price G. D. (1990) Computer modelling of solid-state inorganic materials. *Nature* **347**, 243–248.

Catlow C. R. A., Corish J., Jacobs P. W. M., and Lidiard A. B. (1981), The thermodynamics of characteristic defect parameters. *J. Phys. C: Solid State Phys.* **14**, L121–L125.

Colson R. O., McKay G. A., and Taylor L. A. (1989) Charge balancing of trivalent trace elements in olivine and low-Ca pyroxene: A test using experimental partitioning data. *Geochim. Cosmochim. Acta* **53**, 643–648.

Dick B. G. and Overhauser A. W. (1958) Theory of the dielectric constants of alkali halide crystals. *Phys. Rev.* **112**, 90–103.

Fuller R. G. (1972) Ionic conductivity (including self-diffusion). In *Point Defects in Solids* (ed. J. H. Crawford, Jr. and L. M. Slifkin), Chapter 20. Plenum Press.

Goldschmidt V. M. (1937) The principles of the distribution of chemical elements in minerals and rocks. *J. Chem. Soc., London* **140**, 655–673.

Hauri E. K., Wagner T. P., and Grove T. L. (1994) Experimental and natural partitioning of Th, U, Pb and other trace elements between garnet, clinopyroxene and basaltic melts. *Chem. Geol.* **117**, 149–166.

Hart S. R. and Dunn T. (1993) Experimental cpx/melt partitioning for 24 trace elements. *Contrib. Mineral. Petrol.* **113**, 1–8.

Hazen R. M. and Finger L. W. (1979) Bulk modulus-volume relationship for cation-anion polyhedra. *J. Geophys. Res.* **84**, 6723–6728.

Henderson L. M. and Kracek F. C. (1927) The fractional precipitation of barium and radium chromates. *J. Amer. Chem. Soc.* **49**, 739–749.

Kennedy A. K., Lofgren G. E., and Wasserburg G. J. (1993) An experimental study of trace element partitioning between olivine, orthopyroxene, and melt in chondrules: Equilibrium values and kinetic effects. *Earth Planet. Sci. Lett.* **115**, 177–195.

Kröger F. A. and Vink H. J. (1956) Relations between the concentrations of imperfections in crystalline solids. *Solid State Phys.* **3**, 307–435.

LaTourette T., Hervig R. L., and Holloway J. R. (1995) Trace element partitioning between amphibole, phlogopite and basanite melt. *Earth Planet. Sci. Lett.* **135**, 13–30.

Lewis G. V. and Catlow C. R. A. (1985) Potential models for ionic oxides. *J. Phys.: Solid State Phys.* **18**, 1149–1161.

Levien L. and Prewitt C. T. (1981) High-pressure structural study of diopside. *Amer. Mineral.* **66**, 315–323.

Lidiard A. B. (1989) The Mott-Littleton method: An introductory survey. *J. Chem. Soc., Faraday Trans. II* **85**, 341–349.

Lindstrom D. J. (1976) Experimental study of the partitioning of

the transition metals between clinopyroxene and coexisting silicate liquids. Ph.D. thesis, Univ. Oregon.

Mott N. F. and Littleton M. T. (1938) Conduction in polar crystals. I. Electrolytic conduction in solid salts. *Trans. Faraday Soc.* **34**, 485–499.

Navrotsky A. (1994) *Physics and Chemistry of Earth Materials.* Cambridge Univ. Press.

Onuma N., Higuchi H., Wakita H., and Nagasawa H. (1968) Trace element partition between two pyroxenes and the host lava. *Earth Planet. Sci. Lett.* **5**, 47–51.

Patel A., Price G. D., and Mendelssohn M. (1991) A computer simulation approach to modelling the structure, thermodynamics and oxygen isotope equilibria of silicates. *Phys. Chem. Minerals* **17**, 690–699.

Pavlides P. and Catlow C. R. A. (1994) Atom-atom potential energy calculations for the absorption of cations in muscovite. *Molecular Phys.* **81**, 1269–1279.

Pun A. and Papike J. J. (1995) Ion microprobe investigation of exsolved pyroxenes in cumulate eucrites: Determination of selected trace-element partition coefficients. *Geochim. Cosmochim. Acta* **59**, 2279–2289.

Purton J. A., Allan N. L., Blundy J. D., and Wasserman E. A. (1996) Isovalent trace element partitioning between minerals and melts: A computer simulation study. *Geochim. Cosmochim. Acta* **60**, 4977–4987.

Sanders M. J., Leslie M., and Catlow C. R. A. (1984) Interatomic potentials for SiO_2. *J. Chem. Soc. Chem. Commun.*, 1271–1273.

Shannon R. D. (1976) Revised effective ionic radii and systematic studies of interatomic distances in halides and chalcogenides. *Acta Crystallog.* **A32**, 751–767.

Winkler B., Dove M. T., and Leslie M. (1991) Static lattice energy minimisation and lattice dynamics calculations on aluminosilicate minerals. *Amer. Mineral.* **76**, 313–331.

Wood B. J. and Blundy B. J. (1997) A predictive model for rare earth element partitioning between clinopyroxene and anhydrous silicate melt. *Contrib. Mineral. Petrol.* (in press).